Non-inverting and Non-isolated Magnetically Coupled Buck–Boost Bidirectional DC–DC Converter

Alba Rodríguez-Lorente, Andrés Barrado, *Senior Member, IEEE*, Carlos Calderón,
Cristina Fernández, *Member, IEEE*, and Antonio Lázaro, *Member, IEEE*

***Abstract*—A new non-isolated dc–dc converter with non-inverting output and buck–boost operation, named magnetically coupled buck–boost bidirectional (MCB^3) converter, is presented in this article. The MCB^3 passive components arrangement connects the input and output ports getting an equivalent behavior to that of the dual active bridge (DAB) converter, but in a non-isolated topology. This equivalency allows applying Triple Phase Shift (TPS) modulation to MCB^3. TPS is known to minimize conduction losses and to achieve soft switching at any load in the DAB converter. Throughout the article, the features of the DAB converter are used as a reference to show the main features of the proposed converter. Moreover, other modulation strategies based on TPS modulation are used in MCB^3 to operate within the minimum losses path. The multiple operation modes found on the MCB^3 under TPS modulation are identified, classified, and used to find the operating points that minimize the switching and conduction losses over the power range. The analysis is shown for the boost mode that is the worst case design. MCB^3 and DAB topologies are designed and simulated for the same specification to validate the theoretical study. Finally, experimental measurements on 460-W prototypes for both topologies corroborate the equivalent operation and the main features of the MCB^3.**

***Index Terms*—Bidirectional power flow, DC–DC power converters, design optimization, soft switching.**

I. INTRODUCTION

A NON-ISOLATED bidirectional dc–dc energy transfer capability with a buck–boost operation is useful in many power conversion systems and applications, such as photovoltaic systems, dc microgrids, or electric transport [1]–[5], as long as galvanic isolation is not necessary for high-level safety reasons. The energy storage systems included must ensure the continuity of the power supplied to the output in all circumstances, regardless of the input voltage and the transfer direction.

Within the alternatives with non-inverting output, bidirectional single-ended primary-inductor converter (SEPIC)/ZETA converter is an attractive choice, with little input and output current ripple and simple arrangement. However, it has a high passive component count that can be even higher to reduce switching losses, or need of frequency variation [6], [7]. Four switches non-inverting buck–boost (FSBB) converter with two half-bridges and a single inductor is an interesting choice within the same application area. The higher number of MOSFETs compared to simpler topologies, allows soft-switching operation without adding extra components, in exchange for increased control complexity [8], [9]. Several phases of FSBB are considered in [9] to increase efficiency. Also, more recent topologies, as shown in [10], are investigating FSBB modifications to achieve soft-switching operation. Transformerless dual active half-bridge (TLDAB), in [11], has been developed based on a modification of the well-known dual active bridge (DAB) converter [12]. TLDAB converter employs ac power transfer to substantially reduce the energy storage requirement in the magnetic components, which directly impacts the overall power density of the entire system. However, the TLDAB converter requires of variable switching frequency and mandatory snubbers to achieve the soft-switching operation goal.

The commented topologies are summarized in Table I, with additional information regarding the number and type of components, and the efficiency at the referred voltage gain.

To reduce the overall losses with no need for extra component nor frequency variation, and a desirable reduction on the magnetics volume, the magnetically coupled buck–boost bidirectional (MCB^3) converter is proposed.

The MCB^3 converter provides non-inverting non-isolated buck–boost bidirectional features, with a passive component arrangement that forces the current to follow a specific path in an ac power transfer. The proposed passive link of the input and output ports makes the MCB^3 operation analogous to that of the traditional DAB converter. This achieved behavioral equivalence makes the MCB^3 controllable by employing advanced modulation strategies proven to achieve the target features in the DAB converter. In particular, the triple phase shift (TPS) modulation [13], [14] is chosen in this article to obtain soft-switching operation at a fixed frequency in all the MOSFETs of the MCB^3.

Manuscript received September 10, 2019; revised November 29, 2019 and February 9, 2020; accepted March 16, 2020. Date of publication April 1, 2020; date of current version July 20, 2020. This work was supported in part by the Ministry of Economy and Competitiveness and ERDF funds through the Research Project “Energy Storage and Management System for Hybrid Electric Cars based on Fuel Cell, Battery and Supercapacitors” ELECTRICAR-AG-(DPI2014-53685-C2-1-R), and in part by the Research Projects CONEXPOT (DPI2017-84572-C2-2-R) and EPIIOT (DPI2017-88062-R). Recommended for publication by Associate Editor H. H.-C. Iu. *(Corresponding author: Alba Rodríguez-Lorente.)*

The authors are with the Departamento de Tecnología Electrónica, Universidad Carlos III de Madrid, Madrid 28911, Spain (e-mail: alba.rodriguez@uc3m.es; andres.barrado@uc3m.es; ccaldero@ing.uc3m.es; cfernand@ing.uc3m.es; alazaro@ing.uc3m.es).

Color versions of one or more of the figures in this article are available online at http://ieeexplore.ieee.org.

Digital Object Identifier 10.1109/TPEL.2020.2984202

TABLE I
SUMMARY OF THE CONSIDERED DC–DC NON-ISOLATED BUCK–BOOST TOPOLOGIES

Topology	**MOSFETs**	**Passive Components** (of which magnetics)	**Soft Switching**	**Control Flexibility**	**Efficiency**	**Voltage gain** (Boost operation)
SEPIC/ZETA *w/extra comp.* [6]	4	7 (3)	Yes	Low	90%	2.01
SEPIC/ZETA [7]	2	3(2)	Yes $^{(1)}$	Low	90%	2.67
FSBB [9]	4 $^{(2)}$	1 (1) $^{(2)}$	Yes	Medium	96% $^{(2)}$	2
ZVS-NIBB [10]	4	9 (3)	Yes	Low	94%	1
TLDAB [11]	8	4 (2)	Yes $^{(1)}$	Low	82.5%	3.6

$^{(1)}$Variable frequency. $^{(2)}$Referred to single-phase module.

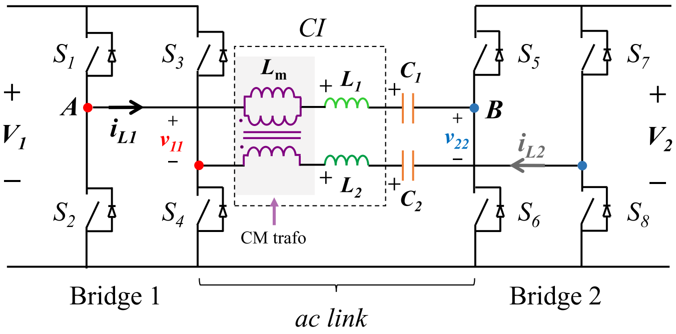

Fig. 1. Proposed MCB^3 converter.

ac link of the proposed MCB^3

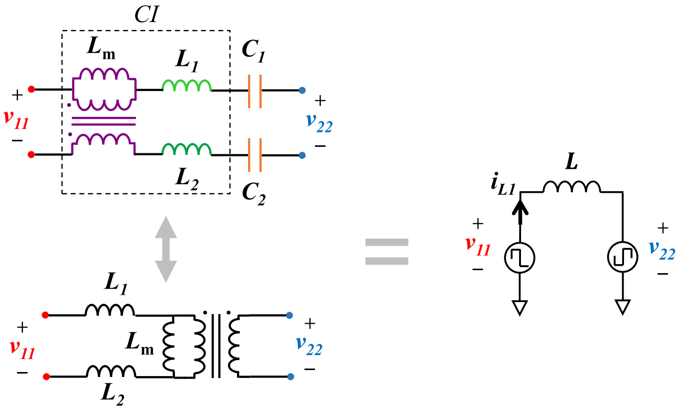

DAB *ac link*

Fig. 2. (a) AC links of MCB^3 and DAB converters. (b) Simplified circuit.

Additionally, minimum conduction losses can be achieved for the entire power range. Moreover, ac power transfer is exploited to save volume on the magnetic components.

The rest of the article is organized as follows. The MCB^3 converter derivation and operating principle are explained in Section II. The different operation possibilities regarding the use of TPS modulation are classified in Section III, together with the procedure to derive the rms current expressions in steady-state operation. In Section IV, the power losses reduction mechanisms applied are discussed, involving soft-switching operation and conduction losses minimization. In Section V, the volts·second in the windings of the magnetic coupling component is studied to size the magnetizing inductance value, so the operation remains close to the ideal one. Simulation and experimental results for the worst case design scenario are presented in Section VI, along with the results obtained for a DAB prototype for the same specification, to validate both the feasibility of the proposal and the hypothesis of behavioral equivalency between them. Finally, Section VII concludes this article.

II. TOPOLOGY DERIVATION AND BASIC OPERATION PRINCIPLE

The circuit of the proposed MCB^3 converter is shown in Fig. 1. The power stage includes two full bridges (Bridges 1 and 2), which generate two ac differential signals (v_{11} and v_{22}) and an *ac link*, comprising the main passive components. This *ac link* is composed of two series capacitors C_1 and C_2 to block the dc component in the *ac link,* and a coupled inductor (CI), which manages and transfers the power between the two bridges. Providing a strong magnetic coupling in the CI windings and the location of the corresponding terminals, the current through the upper branch of the *ac link*, i_{L1}, will have the same value and opposite sign to that through the lower branch, i_{L2}, resulting in no return current through the ground line between the two bridges. The way the CI along with the blocking capacitors connects the input and output full bridges, it produces an analogous operation to the *ac link* in the traditional DAB converter (see Fig. 2) [12]. Although traditionally the DAB converter is represented with a single inductor, in Fig. 2 it has been split in L_1 and L_2 to ease the comparison of the two topologies.

Unless otherwise specified, to ease the theoretical analysis discussed in this article, CI is decomposed into a common mode (CM) transformer, with turns ratio equal to 1, and two discrete inductors L_1 and L_2. The equations of the voltages in *ac link* components are shown in (1)–(3). The value of the capacitors equal ($C_1 = C_2$) and assumed to be large enough to consider constant the voltage across them. The value of magnetizing inductance L_m of the CM transformer is considered as infinite to recreate an ideal coupling

$$v_T = v_A - v_B - (v_{L1} + V_{C1}) \tag{1}$$

$$v_{L1} = v_{L2} = (v_{11} - v_{22})/2 \tag{2}$$

$$V_{C1} = (V_1 - V_2)/2. \tag{3}$$

Analyzing the circuit, as ideally i_{L1} equals i_{L2}, the voltages across C_1 and C_2 cancel each other as well as the voltages in the primary and secondary windings of the CM transformer, as the turn ratio is 1. Hence, the voltage across the inductors only depends on the differential voltages v_{11} and v_{22}. Besides, by considering a strong coupling, inductors L_1 and L_2 act as whether they were in series, hence forming an equivalent inductor L with the value equal to the sum of them. Fig. 2(b) represents the simplified version of the described operation, reducing all the *ac link* passive components to an only inductor L. From this analysis, it is deduced that the operation of the MCB^3 converter is mainly based on the ac energy transference from one bridge to the other throughout a strongly inductive impedance (represented by L), as a consequence of the voltage differences applied between its terminals.

Notice that the proposed converter acts as a current source. Therefore, the voltage gain is settled indirectly by the current transferred from the input to the output port.

III. STEADY-STATE ANALYSIS WITH TPS

As said, the operation of the proposed converter depends mainly on the differential voltages created by the full-bridges' operation. As the simplified structure, as well as the operation, reminds of that of the well-known DAB converter [12], advanced control strategies proven to enhance the DAB features can be taken into consideration to drive MCB^3.

Among the DAB converter control strategies in the literature, phase shift is the most straightforward scheme to be used.

In PS modulation, duty cycles D_1 and D_2 are set to 1, $T_{sw}/2$, being D_1 the Bridge 1 duty cycle defined on the differential signal v_{11}. Equivalently, D_2 is the Bridge 2 duty cycle defined on v_{22} (see Fig. 3) [16].

The two legs in each full bridge are 180º shifted.

The phase shift between MOSFETs S_1–S_2 (outer leg of Bridge 1) and S_5–S_6 (inner leg of Bridge 2) or, equivalently, the angle φ (in radians) between differential voltages v_{11} and v_{22}, is the only control parameter in the PS modulation. This phase shift angle φ is then in charge of control the power transfer, and the transfer direction from Bridge 1 to Bridge 2 when φ is positive, and from Bridge 2 to Bridge 1 when it is negative. However, the performance of the PS is reduced when the ratio V_2/V_1 differs from 1 [12] as the soft-switching operation is lost at light load.

TPS modulation fixes some issues of PS control strategy, acting on up to three control parameters (D_1, D_2, and φ) to improve the controllability of the converter. TPS modulation extends the soft-switching region to the whole power range independently of the ratio V_2/V_1 and allows to minimize the rms current demand by adequately shaping the inductor current profile [13]–[15]. For the reasons given, TPS modulation is chosen to drive the proposed converter.

Fig. 3 shows the main steady-state waveforms for a generic TPS operating point in the proposed MCB^3 converter. Driving signals are shown in gray; differential voltages v_{11} and v_{22} in blue and red, respectively; inductor L_1 voltage and current in green and black; CM transformer voltage current in purple, and C_1 voltage in orange. Neither deadtime nor losses are considered in the representation. Driving signals with a top bar are complementary to the real driving signal.

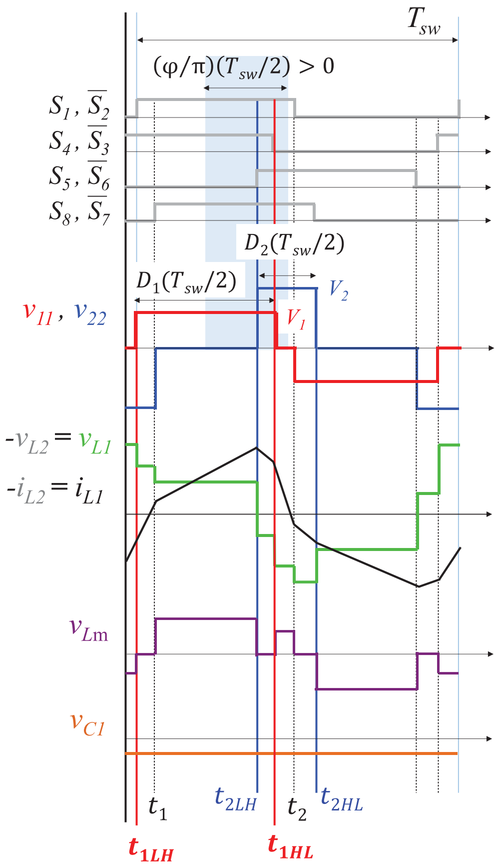

Fig. 3. MCB^3 converter steady-state waveforms in boost operation with TPS.

The possible scenarios that appear when combining voltages V_1 and V_2, with the duty cycles D_1 and D_2, were classified in [16] for the DAB converter with TPS modulation. The same classification criterion is used for the MCB^3: *Case* 1 if $V_1 \geq V_2$ and $D_1 > D_2$; *Case* 2 if $V_1 \geq V_2$ and $D_1 \leq D_2$; *Case* 3 if $V_1 < V_2$ and $D_1 > D_2$; and *Case* 4 if $V_1 < V_2$ and $D_1 \leq D_2$. Notice that the change from *Case* 1 to *Case 4*, and from *Case 2* to *Case 3* is easily done when needed, by changing duty cycles as appropriate.

This article analyzes MCB^3 boost operation in *Case 3*, and Bridge 1 to 2 transfer. Boost operation represents the worst case design with a higher circulating current than equivalent buck operation for a given load. Within the boost operation alternatives, *Case 3* is preferred as it allows soft-switching operation in the whole power range (explanation in Section IV).

As shown in Fig. 3, when an edge appears on signals v_{11} and v_{22}, the slope in the inductor current waveform changes. The way these slopes change produces up to 14 current profiles, named switching modes (SMs). These 14 SMs are identified in [16] for the DAB converter as well, through the progressive increase of the angle φ from $-\pi$ to π. Seven each direction. The same SMs have appeared once applied the described identification procedure to the analyzed MCB^3 converter. The seven SMs found within the direction considered are named as SM$_1$, SM$_2$, SM$_3$, SM$_4$, SM$_5$, SM$_2$*, and SM$_3$*. SM$_2$* and SM$_3$* occur for $D_1 \geq 1\text{-}D_2$ in *Cases 1* and 2, or $D_2 \geq 1\text{-}D_1$ in *Cases 3* and *4*. Their nonasterisked homonyms occur for $D_1 \leq 1\text{-}D_2$. Fig. 4 depicts the seven SMs for *Case 3* and positive φ.

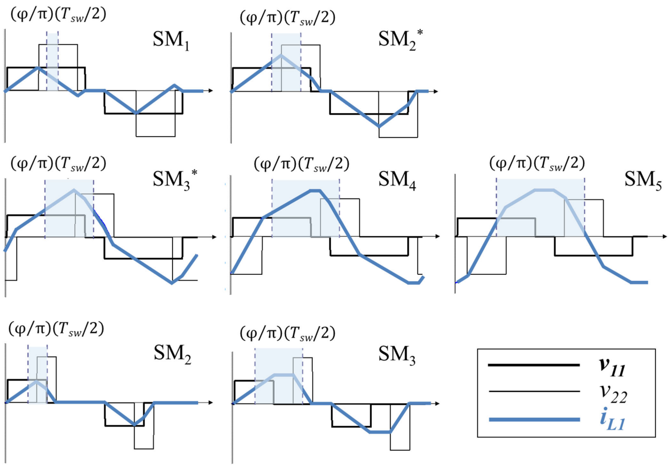

Fig. 4. Example of the SMs current profiles for $0<\varphi<\pi$.

TABLE II

SM RANGE AND POWER EXPRESSIONS IN CASE 3

SM	Range	Power
SM$_1$	$\left(0, \frac{D_1-D_2}{2/\pi}\right]$	$\frac{V_1 \cdot V_2 \cdot D_2(\varphi/\pi)}{2 \cdot f_{sw} \cdot L}$
SM$_2$	$\left(\frac{D_1-D_2}{2/\pi}, \frac{D_1+D_2}{2/\pi}\right]$	$\frac{V_1 \cdot V_2}{4 f_{sw} \cdot L}\left(\frac{\varphi}{\pi}\left(D_1+D_2-\frac{\varphi}{\pi}\right) - \frac{(D_1-D_2)^2}{4}\right)$
SM$_2$*	$\left(\frac{D_1-D_2}{2/\pi}, 1-\frac{D_1+D_2}{2/\pi}\right]$	
SM$_3$	$\left(\frac{D_1+D_2}{2/\pi}, 1-\frac{D_1+D_2}{2/\pi}\right]$	$\frac{V_1 \cdot V_2 \cdot D_2 \cdot D_1}{4 \cdot f_{sw} \cdot L}$
SM$_3$*	$\left(1-\frac{D_1+D_2}{2/\pi}, \frac{D_1+D_2}{2/\pi}\right]$	$\frac{V_1 \cdot V_2}{2 f_{sw} \cdot L}\left(\frac{\varphi}{\pi}\left(1-\frac{\varphi}{\pi}\right) - \frac{(D_1-1)^2+(D_2-1)^2}{4}\right)$
SM$_4$	$\left(1-\frac{D_1+D_2}{2/\pi}, 1-\frac{D_1-D_2}{2/\pi}\right]$	$\frac{V_1 \cdot V_2}{4 f_{sw} \cdot L}\left(\left(1-\frac{\varphi}{\pi}\right)\left(D_1+D_2+\frac{\varphi}{\pi}-1\right) - \frac{(D_1-D_2)^2}{4}\right)$
SM$_5$	$\left(1-\frac{D_1-D_2}{2/\pi}, 1\right]$	$\frac{V_1 \cdot V_2 \cdot D_2(1-(\varphi/\pi))}{2 f_{sw} \cdot L}$

TABLE III

INSTANTANEOUS CURRENT EXPRESSIONS IN CASE 3

SM	Instantaneous current
SM$_1$	$i_{L1}(t_{1LH}) = -i_{L1}(t_{1HL}) = -\frac{D_1 \cdot V_1 - D_2 \cdot V_2}{4 f_{sw} \cdot L}$ $i_{L1}(t_{2LH}) = -\frac{D_2 \cdot V_1 - 2V_1(\varphi/\pi) - D_2 \cdot V_2}{4 f_{sw} \cdot L}$ $i_{L1}(t_{2HL}) = \frac{D_2 \cdot V_1 + 2V_1(\varphi/\pi) - D_2 \cdot V_2}{4 f_{sw} \cdot L}$
SM$_2$ and SM$_{2*}$	$i_{L1}(t_{1LH}) = -i_{L1}(t_{2HL}) = -\frac{D_1 \cdot V_1 - D_2 \cdot V_2}{4 f_{sw} \cdot L}$ $i_{L1}(t_{2LH}) = -\frac{D_2 \cdot V_1 - 2V_1(\varphi/\pi) - D_2 \cdot V_2}{4 f_{sw} \cdot L}$ $i_{L1}(t_{1HL}) = \frac{D_1 \cdot V_1 + 2V_2(\varphi/\pi) - D_1 \cdot V_2}{4 f_{sw} \cdot L}$
SM$_3$	$i_{L1}(t_{1LH}) = -i_{L1}(t_{2HL}) = -\frac{D_1 \cdot V_1 - D_2 \cdot V_2}{4 f_{sw} \cdot L}$ $i_{L1}(t_{1HL}) = i_{L1}(t_{2LH}) = \frac{D_2 \cdot V_2 + D_1 \cdot V_1}{4 f_{sw} \cdot L}$
SM$_{3*}$	$i_{L1}(t_{1LH}) = -\frac{D_1 \cdot V_2 - 2V_2(1-(\varphi/\pi)) + D_1 \cdot V_1}{4 f_{sw} \cdot L}$ $i_{L1}(t_{1HL}) = \frac{D_1 \cdot V_1 + 2V_2(\varphi/\pi) - D_1 \cdot V_2}{4 f_{sw} \cdot L}$ $i_{L1}(t_{2LH}) = -\frac{D_2 \cdot V_1 - 2V_1(\varphi/\pi) - D_2 \cdot V_2}{4 f_{sw} \cdot L}$ $i_{L1}\left(t_{2HL} - \frac{T_{sw}}{2}\right) = \frac{D_2 \cdot V_2 - 2V_1(1-(\varphi/\pi)) + D_2 \cdot V_1}{4 f_{sw} \cdot L}$
SM$_4$	$i_{L1}(t_{1HL}) = i_{L1}(t_{2LH}) = \frac{D_2 \cdot V_2 + D_1 \cdot V_1}{4 f_{sw} \cdot L}$ $i_{L1}(t_{1LH}) = -\frac{D_1 \cdot V_2 - 2V_2\left(1-(\varphi/\pi)\right) + D_1 \cdot V_1}{4 f_{sw} \cdot L}$ $i_{L1}\left(t_{2HL} - \frac{T_{sw}}{2}\right) = \frac{D_2 \cdot V_2 - 2V_1\left(1-(\varphi/\pi)\right) + D_2 \cdot V_1}{4 f_{sw} \cdot L}$
SM$_5$	$i_{L1}(t_{1LH}) = -i_{L1}(t_{1HL}) = -\frac{D_2 \cdot V_2 + D_1 \cdot V_1}{4 f_{sw} \cdot L}$ $i_{L1}\left(t_{2LH} - \frac{T_{sw}}{2}\right) = -\frac{D_2 \cdot V_2 + 2V_1(1-(\varphi/\pi)) + D_2 \cdot V_1}{4 f_{sw} \cdot L}$ $i_{L1}\left(t_{2HL} - \frac{T_{sw}}{2}\right) = \frac{D_2 \cdot V_2 - 2V_1\left(1-(\varphi/\pi)\right) + D_2 \cdot V_1}{4 f_{sw} \cdot L}$

Every SM found has its output power definition. Table II lists the angle φ range for each SM and the corresponding power expression. According to the SM ranges in Table II, the operating point represented in Fig. 3 is classified as SM$_3$*.

Different rms current expressions exist for every SM. Table III lists the i_{L1} current expression at the *reference switching instants*, which are those time instants that delimit the duty cycles D_1 ($t_{1\mathrm{LH}}$ and t_{1HL}) and D_2 ($t_{2\mathrm{LH}}$ and t_{2HL}).

Equations (4)–(7) define the *reference switching instants* based on the control parameters of TPS modulation

$$t_{1LH} = T_{sw} \cdot (1 - D_1)/4 \tag{4}$$

$$t_{1\mathrm{HL}} = T_{sw} \cdot (1 + D_1)/4 \tag{5}$$

$$t_{2LH} = T_{sw} \cdot (2\varphi/\pi + 1 - D_2)/4 \tag{6}$$

$$t_{2\mathrm{HL}} = T_{sw} \cdot (2\varphi/\pi + 1 + D_2)/4. \tag{7}$$

The first four switching instants appearing from the beginning of the period are enough to describe the complete waveform since it is symmetrical. If the needed switching instants do not match with any of the *reference switching instants*, it is possible to obtain the required instant as a linear combination from them (e.g., in Fig. 3, t_1 would be equivalent to t_{2HL}–T$_{sw}/2$, and t_2 as $t_{1LH} + T_{sw}/2$).

The given index to the *reference switching instants* is intended to identify them in any waveform along with this article, as this index defines the change produced in waveforms v_{11} or v_{22} (e.g., in t_{1LH}, number 1 means that it defines a change in waveform v_{11}, and LH refers to the low-to-high edge in the positive half of the v_{11} waveform).

From the information in Table II**,** the i_{L1rms} current is obtained with (8). To found it systematically, t_{ini} must be replaced by the first rising edge time that occurred for v_{11} or v_{22}, during the first half-period. t_{half} must be replaced by the fourth switching instant of v_{11} or v_{22} from the previously settled t_{ini}. The time-lapse between t_{ini} and t_{half} describes a half-period of the current waveform. The procedure includes the partial integration of the instantaneous current. An example of this procedure applied to i_{L1} in Fig. 3 is shown in (9)

$$i_{L1\ \mathrm{rms}}{}^2 = \frac{2}{T_{sw}} \int_{t_{\mathrm{ini}}}^{t_{\mathrm{half}}} i_{L1}(t)^2 dt \tag{8}$$

$$\begin{aligned} i_{L1\ \mathrm{rms}}{}^2 &= \frac{2}{T_{sw}} \int_{t_{1LH}}^{t_2} i_{L1}(t)^2 dt \\ &= \frac{2}{T_{sw}} \left(\int_{t_{1LH}}^{t_1} i_{L1}(t)^2 dt + \int_{t_1}^{t_{2LH}} i_{L1}(t)^2 dt \right. \\ &\quad \left. + \int_{t_{2LH}}^{t_{\mathrm{1HL}}} i_{L1}(t)^2 dt + \int_{t_{\mathrm{1HL}}}^{t_2} i_{L1}(t)^2 dt \right). \end{aligned} \tag{9}$$

IV. LOSSES MINIMIZATION MECHANISMS

In this section, the different mechanisms involving losses minimization in the proposed converter are discussed, exploiting TPS modulation. The goal is to simultaneously reduce the switching and the conduction losses, without the need for frequency variation nor added components.

The traditional DAB converter is commonly designed so that the input-output voltage ratio matches the transformer turn ratio, thus achieving zero-voltage switching (ZVS) operation [12]. However, according to [16], the appliance of (10) allows for soft-switching operation regardless of the turns ratio *n* for any load. Then, *n* becomes an extra freedom degree

$$D_1 \cdot V_1 \cdot n = D_2 \cdot V_2. \tag{10}$$

Once more, since the MCB^3 structure and operation principle allows for taking advantage of the strengths of the DAB advanced modulation strategies, the application of (10) achieves soft-switching operation in the proposed converter. In *Case 3* (boost operation) described, (10) is met in the MCB^3 converter providing *n* equals 1.

The modulation strategy used to drive the proposed MCB^3 converter, starts with $D_1 = D_2 = 0$, for any phase shift φ. D_1 value is gradually increased from 0 to 1. D_2 is then obtained with D_1 and (10). According to the proposals in [13] and [15], once $D_1 = 1$, it remains set to 1, and only D_2 is variated. The resultant TPS modulation pattern is equivalent to the extended phase shift modulation [17], [18]. From that set-point, following with the gradual increase of D_2, eventually, it will also reach 1, from when the control only will vary φ. This last TPS pattern recreates traditional PS modulation [12]. As both extended phase shift modulation (EPS) and PS modulation are particularizations of TPS, then the expressions in Tables II and III are valid for all the three modulation schemes.

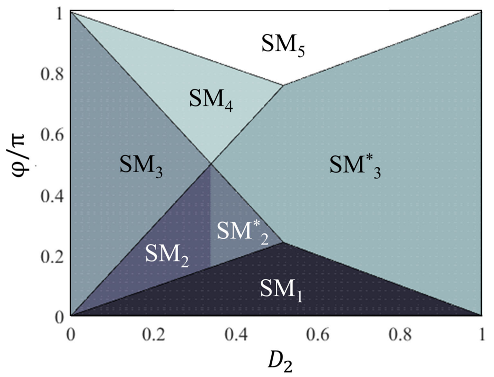

Fig. 5. SM distribution map applied (10) for a given V_1/V_2.

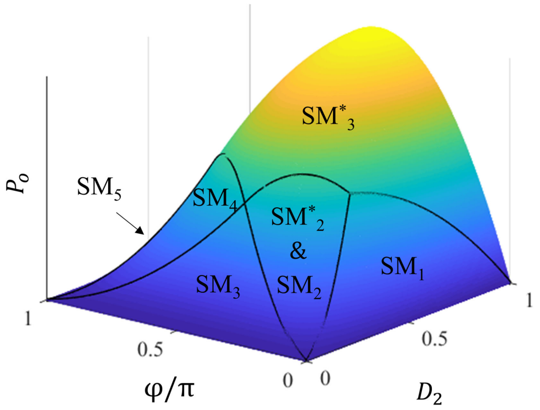

Fig. 6. Power surface for the proposed converter in Case 3.

Fig. 5 shows the seven SM areas for a given V_1/V_2 ratio, as a function of φ and D_2. The duty cycle D_1 is deduced from (10) if D_2 is lower than (V_1/V_2), or equal to 1 otherwise.

For any combination of D_1-D_2-φ, a value of power P_o, and rms current i_{L1} are obtained, by substituting the three variables considered into the corresponding equations.

Fig. 6 shows the surface composed by power values obtained with equations in Table II for every specific D_1-D_2-φ set. Maximum output power $P_{\max}$ occurs at $D_1 = D_2 = 1$ and $\varphi = \pi/2$, which corresponds to SM$_3{}^*$, in Figs. 5 and 6.

The conduction losses reduction is approached from a minimization in the rms current through the upper inductor, i_{L1}. In [13]–[15], the possibility of operating with minimum rms i_{L1} for any load is considered. Thanks to the flexibility offered by the number of control parameters in TPS modulation, there are several parameters set D_1-D_2-φ that get the same power value, with different rms i_{L1} value.

To clarify this concept, Fig. 7 shows two three-dimensional plots ($D_2 - P_o - \varphi$ and $D_2 - i_{L1,\mathrm{rms}} - \varphi$). The colored cut-lines in both pictures represent surfaces with the same power.

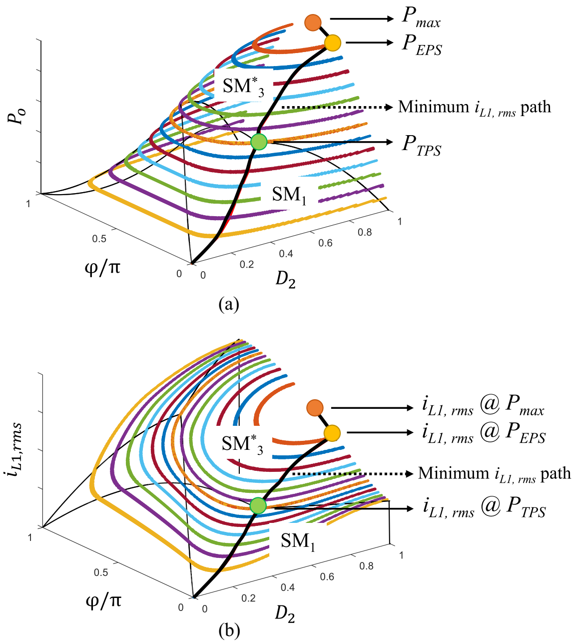

Fig. 7. Constant power surface cuts for (a) power surface and (b) $i_{L1,rms}$ current surface, for the proposed converter in *Case 3*.

A curve made by specific operating points D_1-D_2-φ follows the minimum of each cutline in the surface composed by $D_2 - i_{L1,\mathrm{rms}} - \varphi$. The black curve in plots of Fig. 7 corresponds to the minimum rms current path found.

The green and yellow dots on the surfaces of Fig. 7, P_{TPS} and P_{EPS}, identify the power values when the modulation pattern changes from fully TPS to the equivalent EPS pattern (P_{TPS}), and from EPS equivalent pattern to PS pattern (P_{EPS}). Although it is not mandatory to impose P_{TPS} and P_{EPS} as step values to the algorithm, it helps the accuracy of found path solution for larger grid step sizes.

P_{TPS} limit is obtained by substituting the proper values of D_1-D_2-φ_{TPS} at the power expression of SM$_1$ (see Table II). Phase shift angle φ_{TPS} is calculated from the upper limit equation of SM$_1$; D_1 at P_{TPS} is 1, and D_2 is obtained from (10).

P_{EPS} points to the end of the EPS pattern and the start of the PS equivalent pattern. To find it: first, being D_1 equals 1, the φ_{EPS} expression is derived as a function of D_2 and P_o from SM$_3$* power expression (see Table II).

Next, φ_{EPS} is replaced into the correspondent i_{L1rms} expression for SM$_3$*, which is found following the procedure described in Section III. The $i_{L1,\mathrm{rms}}$ expression is then derived for D_2 and equalized to zero, to obtain the curve made of all the operating points with minimum $i_{L1,\mathrm{rms}}$ in the EPS equivalent pattern. Finally, P_{EPS} is calculated particularizing the result for $D_2 = 1$. The described procedure is based on the proposal in [15] for the traditional DAB converter.

Equations (11) and (12) are the expressions of P_{TPS} and P_{EPS}, found following the described procedure for MCB^3 in *Case 3*, with P_b and r defined by (13) and (14), respectively

$$P_{\mathrm{TPS}} = (P_b/r) \cdot (r-1)/2 \tag{11}$$

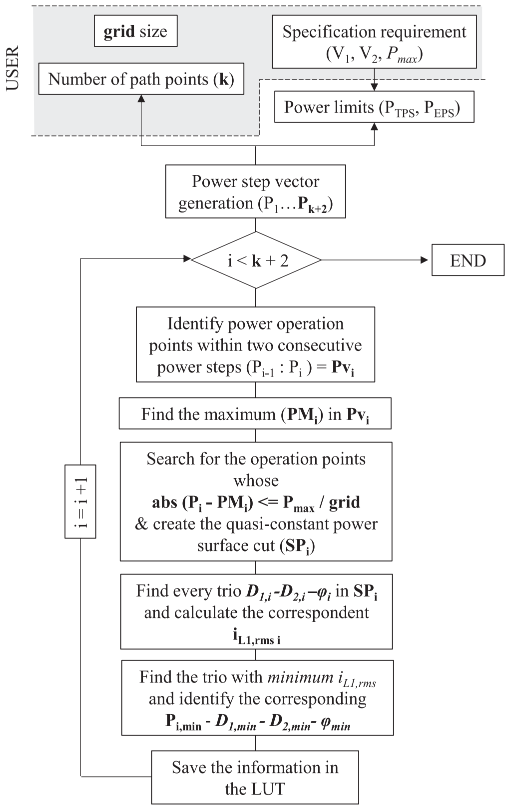

Fig. 8. Minimum $i_{L1,rms}$ path search algorithm flowchart.

$$P_{\mathrm{EPS}} = 0.5 \cdot (-P_b \cdot r) \cdot \left(r^2 - 1 - r\sqrt{r^2-1}\right) \tag{12}$$

$$P_b = V_1^2 / \left(2 \cdot L \cdot f_{sw}\right) \tag{13}$$

$$r = V_2/V_1. \tag{14}$$

Fig. 8 shows the simplified algorithm flowchart proposed to find the preferred minimum rms current path operating points. This offline algorithm results in a look-up table (LUT) compose of the surfaces of values $P_i - D_1 - D_2 - \varphi$ with as many power steps (P_i) as the user sets for the range of voltages settled by the specification requirement. The optimal values of D_1-D_2-φ for any load that does not appear in the table are obtained by interpolation. The use of the proposed search algorithm or simplified equations [16] instead of the exact analytical solution saves computational resources in the case the input specification changes, as the theoretical equations for the minimum rms current path changes with it. If the grid step size is small enough, the difference between the theoretical and the computed minimum rms current path is negligible.

Although the MCB^3 converter close-loop design is beyond the scope of this article, the steps for getting the output voltage control are briefly summarized. The algorithm generates offline the LUT with the data of the control variables, obtained along the minimum rms current path, for a specification V_1-V_2-$P_{\max}$. The V_1 and V_2 voltages and the output current are sensed. The compensator processes the error between V_2 and the voltage reference. The compensator output value is multiplied by the sensed output current to generate P_i. The triad $V_1 - V_2 - P_i$

is used to consult the LUT and obtaining D_1-D_2-φ. Possible changes to the input voltage V_1 are solved by having a surface of multiple paths dependent on V_1, in the LUT.

An increase in L_1 due to the leakage inductance of the CM transformer will reduce the maximum achievable output power, as shown in Table III. There will also be changes in the power and rms current surfaces, both dependent on L_1. Therefore, the control parameters D_1-D_2-φ must be recalculated following the procedure described to transfer the same power, reaching a new minimum rms current. Soft switching is not affected by a change in the value of L_1, according to (10), until P_{TPS} neither after that according to the state-of-the-art [12].

V. VOLTS PER SECOND AT THE CM TRANSFORMER

Until this point, the study of the proposed converter has been based on the consideration of an ideal coupling in the CM transformer that prevents the current returning through the ground line between the two bridges. For the actual case, in which the coupling is not perfect, the L_m value must be controlled so that the ground line current is limited to a small enough value to have a negligible impact on the ideal analysis accomplished.

The volts·second in the MCB^3 CM transformer windings is analyzed over the minimum rms current path operating points, to find a generic equation that helps the transformer sizing, as the volts·second applied to the windings is related with the magnetizing inductance L_m.

Fig. 9 shows three generic operating points for the MCB^3 in *Case 3*, belonging to the preferred minimum rms current path: TPS modulation in Fig. 9(a); EPS modulation in Fig. 9(b); and PS modulation in Fig. 9(c) equivalent patterns, respectively. The colored area represents the volts·second on the CM transformer windings. As seen, the MCB^3 CM transformer voltage, v_{Lm}, is positive when v_{11}, v_{22}, or both are zero.

As shown in Fig. 9(a), in TPS there is a considerable amount of time with $v_{11} = v_{22} = 0$. Therefore, the V·s area will be higher than in the rest of the operating points shown. In Fig. 9(b), with an EPS pattern, the V·s applied is smaller than in Fig. 9(a), since one of the duty cycles is 1. In Fig. 9(c), the value of V·s applied is 0 since there are no periods with zero volts in v_{11} and v_{22}.

Volts·second on a magnetic component windings is obtained applying (15) to the positive part of the voltage waveform

$$\lambda = \int_{t_a}^{t_b} v_{Lm}(t)\ dt. \tag{15}$$

The integration limits t_b and t_a must be replaced by the corresponding values of the switching instants that delimit the waveform v_{Lm}. The process may involve partial integration. Equation (16) is derived for the analyzed *Case 3* and is also valid for *Case 2* if the absolute value is taken.

The maximum value $\lambda_{\mathrm{MCB}^3,\max}$ needed to size L_m is reached at $D_1 = D_2 = 0.5$

$$\begin{aligned}\lambda_{\mathrm{MCB}^3,\ \mathrm{Case\ 3}} &= \frac{T_{sw}}{2}\left(-v_{C1}(1-D_1) + \left(\frac{V_1}{2} - v_{C1}\right)(D_1 - D_2)\right)\\ &= \frac{T_{sw}}{4}\left(V_2(1-D_2) - V_1(1-D_1)\right).\end{aligned} \tag{16}$$

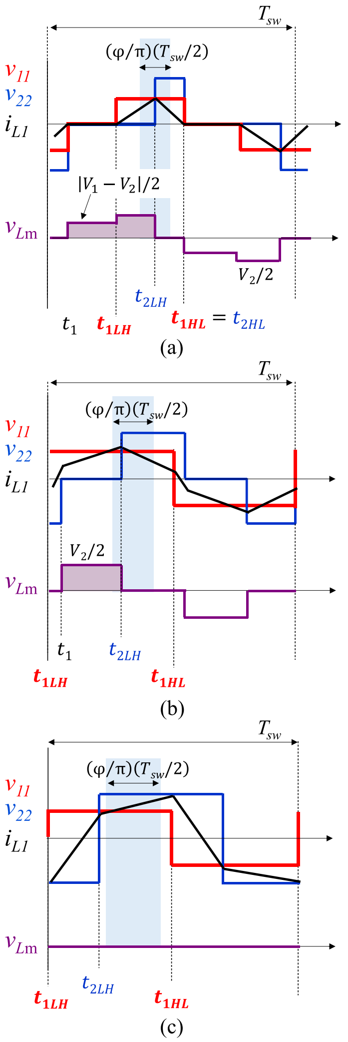

Fig. 9. Volts·second study on the CM transformer over the three equivalent TPS modulation patterns: (a) fully TPS; (b) EPS; and (c) PS.

In this article, the volts-second in the transformer windings of the traditional DAB converter is also considered, to evaluate the impact in terms of volume that would imply the construction of a component with the magnetizing current peak limited by a sufficiently large L_m value. For the DAB converter with the same modulation strategy applied, (17) is the expression for the volts·second in the galvanic isolation transformer windings, as v_{22} will be imposed directly on the isolation transformer windings. In this case, the maximum value $\lambda_{\mathrm{DAB},\max}$ occurs in the PS equivalent pattern at high load

$$\lambda_{\mathrm{DAB}} = \frac{D_2 \cdot (V_2/n)}{2 f_{sw}}. \tag{17}$$

Fig. 10 shows the region where $\lambda_{\mathrm{MCB}^3,\max}$ is smaller than $\lambda_{\mathrm{DAB},\max}$, shadowed area. It can be seen that for any voltage ratio, $\lambda_{\mathrm{MCB}^3,\max}$ is smaller than $\lambda_{\mathrm{DAB},\max}$ for the same combination V_2/V_1 and $n = 1$, which is the turns ratio for the MCB^3 converter's CM transformer. This assertion has a limit at $V_2/V_1 = 1/3$, but it will never correspond to the worst case design at boost operation, then it will not impact on the final power stage design.

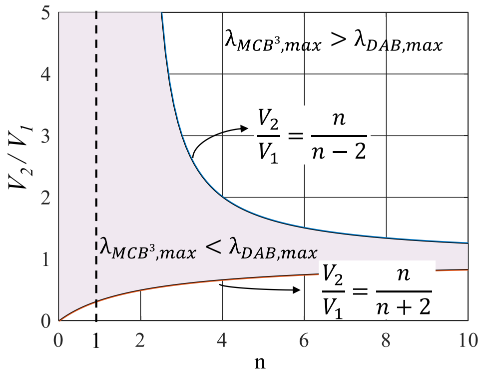

Fig. 10. Maximum volts·second area comparison for MCB^3 CM transformer (λ_{MCB^3}) and DAB transformer (λ_{DAB}).

TABLE IV
SPECIFICATION PARAMETERS

Parameter	Topology	Value
V_1	DAB and MCB^3	**[124, 278] V**
V_2		**240 V**
P_{max}		**460 W**
f_{sw}		**50 kHz**
n		**1**
L_1=L_2	DAB/MCB^3	80 μH
L_m		24 mH /5.8 mH
C_1=C_2	MCB^3	14 μF

VI. TOPOLOGY VALIDATION

In this section, simulation and experimental results are provided to validate the MCB^3 converter theoretical analysis, and to demonstrate that the same enhanced features are achieved by using the described control strategy with DAB and MCB^3 converters. Parameters on Table IV are set for both converters to check the behavioral equivalency. Those parameters MCB^3 in bold are the same for both topologies.

The operation in *Case 3* described is validated with voltage ratios $V_2/V_1 > 1$, which includes the worst case operation.

A magnetizing current peak, Δi_{Lm}, of 0.05 A is taken as a common criterion to design the transformer in both converters, small enough to analyze the MCB^3 converter ideally.

Equation (18) is used to size L_m to keep Δi_{Lm} limited at the desired value, substituting the term $\lambda_{\max}$, with the maximum from (16)

$$L_m = \frac{\lambda_{\max}}{2 \cdot \Delta i_{Lm}}. \tag{18}$$

The value $L_1 = L_2$ is obtained from the power equation of SM$_3{}^*$ in Table II, to get $P_{\max}$ at $D_1 = D_2 = 1$, and $\varphi/\pi = 0.5$. The values are the same for both topologies since the power equations are also the same [16].

The value $C_1 = C_2$ is chosen so that the resonance frequency with the inductances L_1 and L_2, which operate in series, is far away from the switching frequency (at least two decades lower). That way, the impedance of the *ac link* remains strongly inductive at the switching frequency, getting the intended operation.

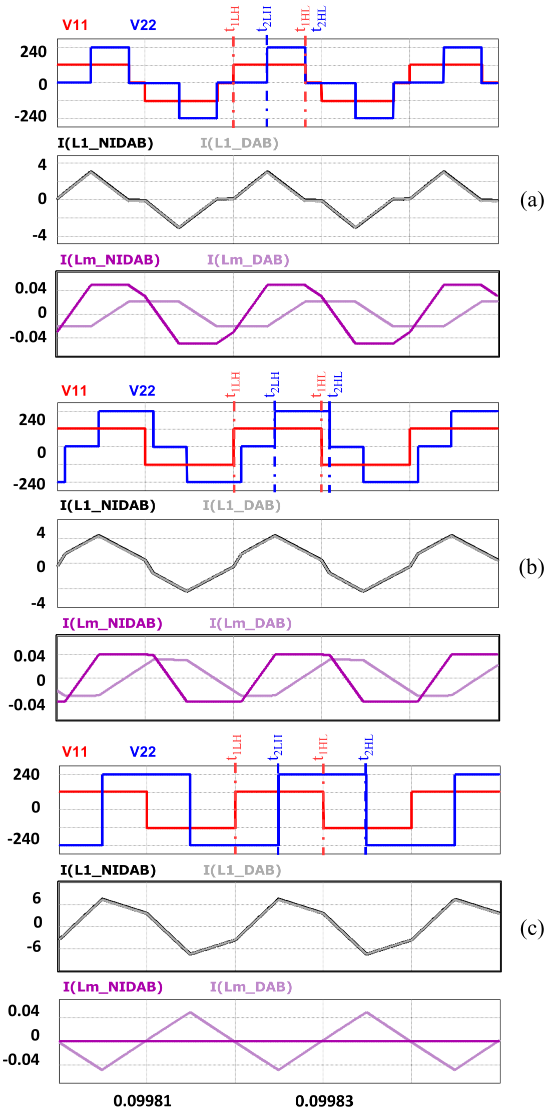

Fig. 11. Simulated waveforms for MCB^3 and DAB converters for (a) TPS at 166 W, (b) EPS at 333 W, and (c) 460 W ($P_{\max}$) at PS.

A. Simulation Results

The simulation of three different operating points belonging to the different modulation patterns (fully TPS, EPS, and PS) in the minimum rms current path is shown in Fig. 11. Each image shows differential full-bridge voltages v_{11} and v_{22}, i_{L1} current in the proposed MCB^3 and the DAB converters, and magnetizing current i_{Lm} in both transformers. The operating points are for 166, 333, and 460 W ($P_{\max}$). Simulation entries are those from Table IV, which reproduce the worst case design, then V_1 and V_2 are 124 and 240 V, respectively ($r = 1.93$).

The control parameters (D_1-D_2-φ) to simulate the chosen operating points with the expected rms inductor current are shown in Table V. Equations to calculate rms i_{L1} (19) and (20) are derived from the procedure described in Section III.

TABLE V
SIMULATION PARAMETERS

Output power	SM	D_1	D_2	φ/π	$i_{L1,rms}$
166 W	SM_1	0.82	0.43	0.19	1.7 A
333 W	SM_3^*	1	0.62	0.28	2.9 A
500 W	SM_3^*	1	1	0.5	5.2 A

TABLE VI
SWITCHING TIME AND SOFT SWITCHING IN THE MOSFETS

Switch	Turn-on time	Soft Switching		Turn-off time	Soft Switching	
		SM_1	SM_3^*		SM_1	SM_3^*
S_1	t_{1LH}	ZCS	ZVS	$t_{1LH} + T_{sw}/2$	ZCS	HS
S_2	$t_{1LH} + T_{sw}/2$	ZCS	ZVS	t_{1LH}	ZCS	HS
S_3	t_{1HL}	ZCS	ZVS	$t_{1HL} + T_{sw}/2$	ZCS	HS
S_4	$t_{1HL} + T_{sw}/2$	ZCS	ZVS	t_{1HL}	ZCS	HS
S_5	t_{2LH}	ZVS	ZVS	$t_{2LH} + T_{sw}/2$	HS	HS
S_6	$t_{2LH} + T_{sw}/2$	ZVS	ZVS	t_{2LH}	HS	HS
S_7	t_{2HL}	ZCS	ZVS	$t_{2HL} + T_{sw}/2$	ZCS	HS
S_8	$t_{2HL} + T_{sw}/2$	ZCS	ZVS	$t_{1LH} + T_{sw}/2$	ZCS	HS

Table VI lists the time instants when the MCB^3 MOSFETs are turned ON and OFF, and the soft-switching type during turning ON. MOSFETs in red are located in Bridge 1, whereas those in blue are in Bridge 2. MOSFETS S_2, S_3, S_5, and S_8 have ZVS, during turning ON, when the inductor current i_{L1} is positive, or zero current switching (ZCS) in case it is zero. In turn, S_1, S_4, S_6, and S_7 have ZVS, during turning ON, when i_{L1} is negative, or ZCS in case it is zero.

Table VI eases the identification of the soft-switching type in the simulation waveforms of Fig. 11, as the turn-ON and turn-OFF instants are described with the *reference switching instants* indexes. These indexes are self-explanatory of the instant when they occurred, as explained in Section III.

The TPS operating point in Fig. 11(a) has D_1 and D_2 smaller than 1, with time intervals where $v_{11} = v_{22} = 0$, and corresponds to an SM_1. MCB^3 and DAB currents i_{L1} are superimposed. This means that TPS modulation shapes the current profile the same for both topologies, so the same benefits will be obtained from its appliance

Thus, the proposed MCB^3 converter has soft switching in all the MOSFETs and the minimum rms current for this power requirement. The represented operating point always has nonzero volts·second applied to the CM transformer windings during the switching period. As D_1 and D_2 are related by (10) during pure TPS, then λ_{MCB^3} remains at a constant value of 0.6 μV·s for any load below P_{TPS}. During this power range, λ_{MCB^3} reaches the maximum, $\lambda_{\mathrm{MCB}^3,\max}$. As seen, Δi_{Lm} reaches 0.05 A at $\lambda_{\mathrm{MCB}^3,\max}$; then, L_m sizing is validated.

Fig. 11(b) shows an EPS equivalent pattern operating point. In this case, the current profile belongs to the $\mathrm{SM}_3{}^*$. i_{L1} in MCB^3 and DAB converters are superimposed, then the modulation strategy will work the same for both converters, getting soft switching and minimum rms current again in all the MOSFETs. MCB^3 and DAB behavioral equivalency is also verified with EPS modulation.

Fig. 11(c) shows the PS operating point at $P_{\max}$. The current profile also belongs to the $\mathrm{SM}_3{}^*$. Even at PS, i_{L1} of both converters are superimposed so, behavioral equivalency with the traditional DAB converter is verified for every modulation scheme tried, and therefore, for the TPS chosen strategy, which combines all the three patterns. As shown in Section V, DAB magnetizing current peak at 0.05 A is at PS equivalent pattern, and zero at the MCB^3, in the same situation. Therefore, the L_m sizing is validated for any load and topology.

B. Experimental Results

A prototype of the proposed MCB^3 converter has been built and tested along with a prototype of the DAB converter to validate the theoretical analysis and simulation, for the specification values of Table IV. Both converters have been

$$
\begin{aligned}
{i_{L1}}^2_{\mathrm{rms},\mathrm{SM1}} = \frac{2}{T_{sw}} \int_{t_{1LH}}^{t_{1\mathrm{HL}}} i_{L1,\,\mathrm{SM1}}(t)^2\, dt = \big[&D_2^3V_1V_2 - 2D_1^3V_1^2 + 3D_1^2V_1^2 + 3D_1^2D_2V_1V_2 - 6D_1D_2V_1V_2 \\
&+12D_1V_1V_2\varphi^2 - 2D_2^3V_2^2 + 3D_2^2V_2^2\big] \cdot \frac{1}{48f_{sw}^2 \cdot (L_1+L_2)^2}
\end{aligned}
\tag{19}
$$

$$
\begin{aligned}
{i_{L1}}^2_{\mathrm{rms},\,\mathrm{SM3^*}} = \frac{2}{T_{sw}} \int_{t_{1LH}}^{t_{1\mathrm{HL}}} i_{L1,\,\mathrm{SM3^*}}(t)^2\, dt = [&3D_1^2V_1^2 - 2D_1^3V_1^2 - 6D_1^2V_1V_2\varphi + 3D_1^2V_1V_2 + 12D_1V_1V_2\varphi \\
&- 6D_1V_1V_2 - 2D_2^3V_2^2 - 6D_2^2V_1V_2\varphi + 3D_2^2V_1V_2 + 3D_2^2V_2^2 + 12D_2V_1V_2\varphi - 6D_2V_1V_2 - 8V_1V_2\varphi^3 + 12V_1V_2\varphi^2 \\
&-12V_1V_2\varphi + 4V_1V_2]\, \frac{1}{48f_{sw}^2 \cdot (L_1+L_2)^2}.
\end{aligned}
\tag{20}
$$

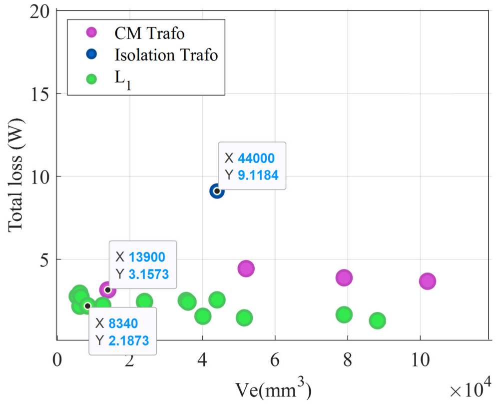

Fig. 12. Magnetic components designs considered.

TABLE VII
MAGNETIC COMPONENTS BUILDING PARAMETERS

Component	Core	Value	Wire section	N_1/N_2	gap
$L_{m,\,DAB}$	E65/32/27	24.5 mH	3x 0.5mm^2	53/53	-
$L_{m,\,MCB^3}$	RM14	5.6 mH	3x 0.5mm^2	30/30	-
$L_1 = L_2$	RM12	80μH	3x 0.5mm^2	28	1.9mm

built using the same layout and same common components (semiconductors, drivers, input and output capacitors, L_1 and L_2 inductors), so the differences are due to the dc blocking capacitors combined with the CM transformer in MCB^3 *ac-link*, compared to the DAB isolation transformer.

The design of the magnetic components follows the standard procedure described in [19], so that the minimum total losses are obtained by finding the optimal flux density for each core size considered. This procedure is applied over the Ferroxcube core database [21] for 3F3 ferrite. Fig. 12 shows the design solutions that comply the basic limitations of window area occupation (set to be less than or equal to 35% as it is handmade) and current density (set to be around 10 A/mm^2). Solutions are located regarding their total magnetic loss in watts (*Y*-axis) compare to their effective volume in cubic millimeters (*X*-axis). Blue dots correspond to the DAB transformer design, purple dots are for MCB^3 CM transformer, and green ones are for inductor L_1. The same inductor design is chosen for the two topologies, as the maximum current and volts·second applied to them are the same. The building parameters are shown in Table VII.

In Fig. 13(a), the full prototype is shown. The promising possibilities for magnetics volume reduction of the proposed MCB^3 converter are highlighted in Fig. 13(b).

The CM transformer is six times smaller than the DAB isolation transformer. The sum of the dc blocking capacitors (KRM55WR72A226MH01L) and the CM transformer volumes represents 18% of DAB's transformer volume. Then, although it is possible to use the DAB converter in non-isolated applications, the proposal saves volume while maintaining the same preferable features.

The measurements on MCB^3 and DAB prototypes are shown in Fig. 14. Fig. 14(a)–(c) corresponds to the MCB^3 converter, whereas Fig. 14(d)–(f) corresponds to the DAB converter. The measurements are done for the operating points in Table V to check whether the experimental results agree with the simulations.

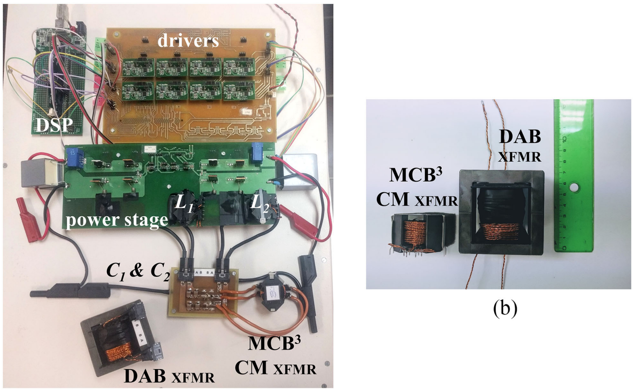

(a)

(b)

Fig. 13. Photographs of (a) experimental prototype set-up, and (b) detail of MCB^3 and DAB transformers.

Differential voltages v_{11} and v_{22} are shown in yellow and gray using the same scale, displayed as *Math1*. Inductor current, i_{L1}, is shown in channel *Ch3* in purple. *Reference switching instants* are shown with a red line (continuous at t_{1LH} and dashed at t_{1HL}) for Bridge 1, and in blue (continuous at $t_{2\mathrm{LH}}$ and dashed at t_{2HL}) for Bridge 2.

TPS operating point is shown in Fig. 14(a) for the MCB^3 converter and in Fig. 14(d) for the DAB converter. As can be seen, the waveforms are much alike to those expected from the corresponding simulation results, in Fig. 11(a).

The EPS equivalent pattern operating point is shown in Fig. 14(b) and (e), for the MCB^3 converter and the DAB converter, respectively. The waveforms are practically identical to those expected from the corresponding simulation [see Fig. 11(b)].

The current peak of 4.5 A is a little higher than obtained in simulation (4.2 A) as the losses are compensated for having the exact output voltage value.

$P_{\max}$ current profiles in Fig. 14(c) and (f) belong to SM_3*. As the last operating point considered, it finishes with the validation of current waveform matching between MCB^3 theoretical analysis, simulation study, and experimental measurements.

The behavioral equivalency of the proposed MCB^3 converter with traditional DAB converter is also wholly verified, as their current profiles match for any load and modulation pattern considered. This feature allows the MCB^3 converter to be further enhanced with any other contributions done in the research for the DAB converter [20].

Fig. 15 shows the efficiency curves of the proposed MCB^3 converter for three different V_1 voltages within the range indicated in Table IV. A maximum efficiency of 95.2% has been reached in the worst case design (highest V_2/V_1 ratio, blue curve), and 97.2% for 200–240 V (input voltage to output voltage, orange curve) for the TPS operation described.

The differences are especially noticeable from medium to high load, where conduction losses become more relevant. Since

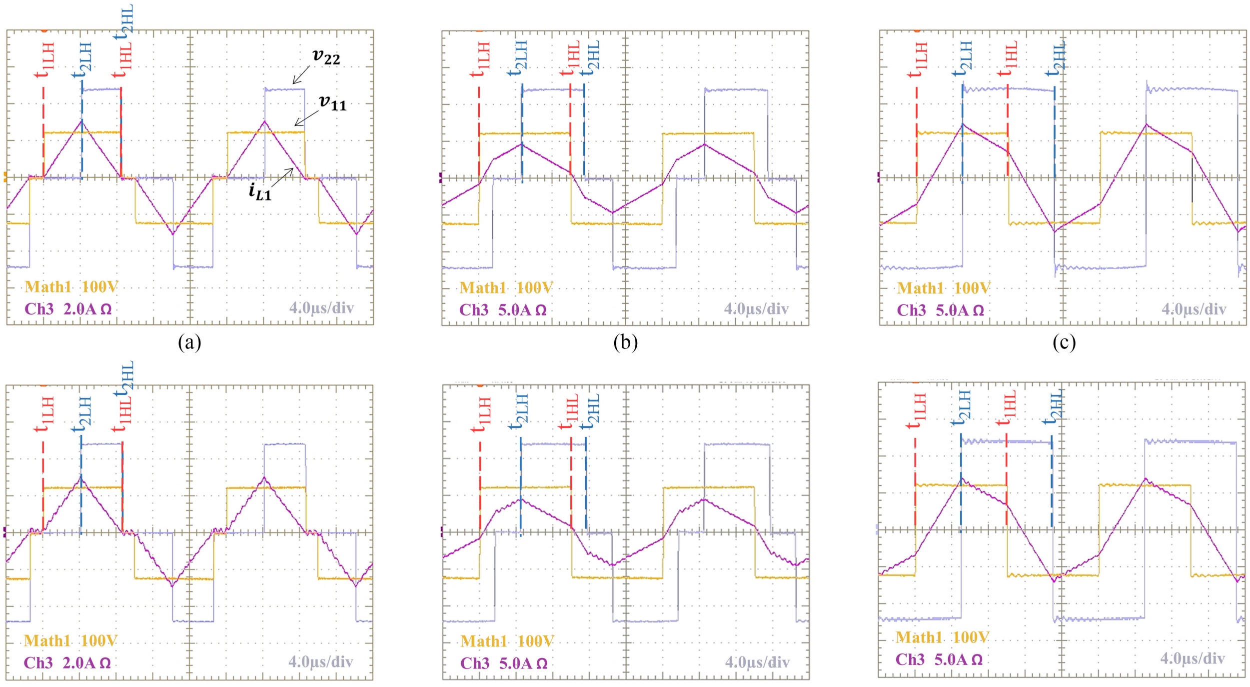

(a) (b) (c)

(d) (e) (f)

Fig. 14. Experimental results of 166 W, 333 W, and $P_{\max}$ for the (a)–(c) MCB^3 converter and for the (d)–(f) DAB converter.

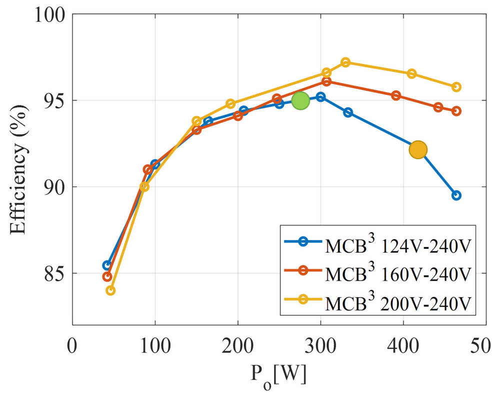

Fig. 15. MCB^3 converter efficiency curves at different input voltages.

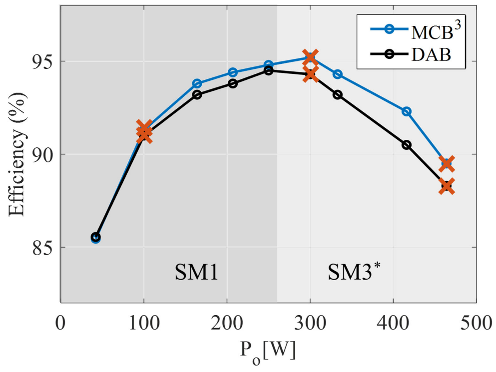

Fig. 16. MCB^3 and DAB converters efficiency curves at $V_1 = 124$ V and $V_2 = 240$ V.

the current to provide the same output power is reduced as the input voltage increases, the losses are lower as well.

In addition, Fig. 15 shows P_{TPS} (green dot) and P_{EPS} (orange dot) occurrence for the MCB^3 converter at the 124–240 V efficiency curve. These dots correspond to the ones shown in Fig. 6.

The traditional DAB converter and MCB^3 efficiency curves for the highest V_2/V_1 ratio (124–240 V) are shown in Fig. 16, for the same TPS operation and the parameters in Table IV. The red crosses point out the waveforms shown in Fig. 14.

The difference in the efficiency between the MCB^3 converter and the DAB converter curves for all power range is due to the DAB transformer's bigger volume. As the magnetizing current peak is fixed by design, core loss depends only on the volume. The efficiency drop in both curves occurs after the SM region changes from SM$_1$ to SM$_3$*, as the number of MOSFETs with hard switching turning OFF increases, as shown in Table VI.

VII. CONCLUSION

A novel buck–boost bidirectional non-isolated topology named MCB^3 converter is presented in this article.

The proposed converter gets soft-switching operation, with no need for variable frequency or snubbers, over the entire load range. The MCB^3 converter operation resembles the one of popular DAB converter, exploiting the ac power transfer operation and getting to better use of the magnetic elements. Thus, the MCB^3 is focused on those applications fields that do not require high-level safety, and therefore do not need galvanic isolation, but in which having the main features of the DAB is an advantage.

TPS modulation is used on the MCB^3 converter for taking advantage of this operation equivalency, as it allows achieving not only the soft-switching operation but also minimum rms current for any power requirement.

The steady-state analysis of the proposed converter and the procedure to derive the rms current expressions is described. General soft-switching operation condition and the procedure to find the minimum rms current path are also provided. The optimal control parameters to achieve the preferred operation are shown.

The volts·second in the CM transformer windings is studied to analyze the magnetic integration possibilities. The volts·second in the DAB converter isolation transformer is considered to emphasize the volume reduction in the proposal when the evaluated components are built to have the same magnetizing current peak. Maximum volts·second in CM transformer remains smaller than those in the DAB isolation transformer for buck–boost voltage gain ratios from 1/3 to 3, providing the turns ratio in the DAB converter is chosen to meet the voltage ratio, as it is commonly recommended to achieve better performance [12].

The simulation results validate the behavioral equivalency of the proposed converter with a traditional DAB converter, for any load and modulation pattern considered during the control strategy used. The prototypes of the MCB^3 and DAB converters are build and tested, sharing the full bridges and the input and output filters to evidence the proposal contributions. MCB^3 converter efficiency remains equal or higher than the DAB's one, with a maximum of about 95%, which is in the same order as the better topology considered in the state-of-art initial research. The passive components total volume in the proposed MCB^3 converter is around one-fifth of those in the DAB converter.

Besides, it is expected that the particularity of the MCB^3 converter to replicate the DAB operation will allow it to improve its performance with other contributions developed for the DAB converter.

REFERENCES

[1] Y. Du, X. Zhou, S. Bai, S. Lukic, and A. Huang, “Review of non-isolated bi-directional DC–DC converters for plug-in hybrid electric vehicle charge station application at municipal parking decks,” in *Proc. IEEE Appl. Power Electron. Conf. Expo.*, 2010, pp. 1145–1151.

[2] M. Bragard, N. Soltau, S. Thomas, and R. W. De Doncker, “The balance of renewable sources and user demands in grids: Power electronics for modular battery energy storage systems,” *IEEE Trans. Power Electron.*, vol. 25, no. 12, pp. 3049–3056, Dec. 2010.

[3] M. Kasper, D. Bortis, and J. W. Kolar, “Classification and comparative evaluation of PV panel-integrated DC–DC converter concepts,” *IEEE Trans. Power Electron.*, vol. 29, no. 5, pp. 2511–2526, May 2014.

[4] K. Tytelmaier, O. Husev, O. Veligorskyi, and R. Yershov, “A review of non-isolated bidirectional dc–dc converters for energy storage systems,” in *Proc. Int. Young Scientists Forum Appl. Phys. Eng.*, 2016, pp. 22–28.

[5] K. Thirugnanam, S. K. Kerk, C. Yuen, N. Liu, and M. Zhang, “Energy management for renewable microgrid in reducing diesel generators usage with multiple types of battery,” *IEEE Trans. Ind. Electron.*, vol. 65, no. 8, pp. 6772–6786, Aug. 2018.

[6] I. D. Kim, S. H. Paeng, J. W. Ahn, E. C. Nho, and J. S. Ko, “New bidirectional ZVS PWM Sepic/Zeta DC–DC converter,” in *Proc. IEEE Int. Symp. Ind. Electron.*, Nov. 2007, pp. 555–560.

[7] B. Ulrich, “Analysis of a ZVS synchronous Sepic/Zeta dc/dc converter,” in *Proc. PCIM Eur. Conf.*, 2018, pp. 1623–1630.

[8] X. Weng *et al.*, “Comprehensive comparison and analysis of non-inverting buck boost and conventional buck boost converters,” *J. Eng.*, vol. 2019, no. 16, pp. 3030–3034, 2019.

[9] S. Waffler and J. W. Kolar, “A novel low-loss modulation strategy for high-power bidirectional buck boost converters,” *IEEE Trans. Power Electron.*, vol. 24, no. 6, pp. 1589–1599, Jun. 2009.

[10] X. F. Cheng, Y. Zhang, and C. Yin, “A zero voltage switching topology for non-inverting buck–boost converter,” *IEEE Trans. Circuits Syst. II, Express Briefs*, vol. 66, no. 9, pp. 1557–1561, Sep. 2018.

[11] A. Amin, M. Shousha, A. Prodic, and B. Lynch, “A transformerless dual active half-bridge DC–DC converter for point-of-load power supplies,” in *Proc. IEEE Energy Convers. Congr. Expo.*, 2015, pp. 133–140.

[12] A. Rodríguez, A. Vázquez, D. G. Lamar, M. M. Hernando, and J. Sebastián, “Different purpose design strategies and techniques to improve the performance of a dual active bridge with phase-shift control,” *IEEE Trans. Power Electron.*, vol. 30, no. 2, pp. 790–804, Feb. 2015.

[13] F. Krismer and J. W. Kolar, “Closed form solution for minimum conduction loss modulation of DAB converters,” *IEEE Trans. Power Electron.*, vol. 27, no. 1, pp. 174–188, Jan. 2012.

[14] J. Huang, Y. Wang, Z. Li, and W. Lei, “Unified triple-phase-shift control to minimize current stress and achieve full soft-switching of isolated bidirectional DC–DC converter,” *IEEE Trans. Ind. Electron.*, vol. 63, no. 7, pp. 4169–4179, Jul. 2016.

[15] C. Calderon, A. Barrado, A. Rodriguez, A. Lazaro, M. Sanz, and E. Olías, “Dual active bridge with triple phase shift, soft switching and minimum RMS current for the whole operating range,” in *Proc. Ann. Conf. IEEE Ind. Electron. Soc.*, 2017, vol. 11, pp. 4671–4676.

[16] C. Calderon *et al.*, “General analysis of switching modes in a dual active bridge with triple phase shift modulation,” *Energies*, vol. 11, no. 9, pp. 2419–2443, 2018.

[17] B. Zhao, Q. Yu, and W. Sun, “Extended-phase-shift control of isolated bidirectional DC–DC converter for power distribution in microgrid,” *IEEE Trans. Power Electron.*, vol. 27, no. 11, pp. 4667–4680, Nov. 2012.

[18] B. Zhao, Q. Song, W. Liu, and Y. Sun, “Overview of dual-active-bridge isolated bidirectional DC–DC converter for high-frequency-link power-conversion system,” *IEEE Trans. Power Electron.*, vol. 29, no. 8, pp. 4091–4106, Aug. 2014.

[19] D. Maksimović and R. W. Erickson, *Fundamentals of Power Electronics*, 2nd ed. New York, NY, USA: Kluwer, 2011.

[20] O. M. Hebala, A. A. Aboushady, K. H. Ahmed, and I. Abdelsalam, “Generic closed-loop controller for power regulation in dual active bridge DC–DC converter with current stress minimization,” *IEEE Trans. Ind. Electron.*, vol. 66, no. 6, pp. 4468–4478, Jun. 2019.

[21] *Soft Ferrites and Accessories—Data Handbook*, Ferroxcube, New Taipei City, Taiwan, 2013.

Alba Rodríguez-Lorente received the M.Sc. degree in electronic systems and applications, in 2015, from the Universidad Carlos III de Madrid, Madrid, Spain, where she is currently working toward the Ph.D. degree in electronic engineering with the Power Electronics Systems Group.

Her research interests include dc–dc switching power converters design, and modeling and optimization of magnetics components.

Andrés Barrado (Senior Member, IEEE) received the M.Sc. degree in electrical engineering from the Polytechnic University of Madrid, Madrid, Spain, in 1994, and the Ph.D. degree from the Universidad Carlos III de Madrid, Madrid, Spain, in 2000.

He is currently a Full Professor with the Universidad Carlos III de Madrid, where he has been the Head of the Power Electronics Systems Group since 2004. He has authored/coauthored more than 200 scientific papers in international journals and conference proceedings and holds 12 patents. He has been actively involved in more than 85 R&D projects for companies in Europe and the USA, and more than 25 projects with public funding, in the field of power electronics. He is the co-founder of a spin-off company “Power Smart Control S.L.” targeting to applications and CAD for power electronics. His research interests include switching-mode power supply, solar and fuel cell conditioning, behavioral modeling of converters and systems, fuel cell electric vehicle, power distribution systems for aircrafts, and electromagnetic compatibility.

Carlos Calderón received the M.Sc. degree from the Universidad Politécnica de Madrid, Madrid, Spain, in 2015. He is currently working toward the Ph.D. degree with the Universidad Carlos III de Madrid, Madrid, Spain.

He works in auxiliary power supply design for the railway industry. His research interests include bidirectional dc–dc switching power converters design, modeling, and control.

Cristina Fernández (Member, IEEE) received the M.Sc. and Ph.D. degrees in electrical engineering from the Universidad Politécnica de Madrid, Madrid, Spain, in 1998 and 2004, respectively.

From 1997 to 2003, she researched in the field of power electronics with the Universidad Politécnica de Madrid. In 2000, she was a Summer Intern with the Center of Research and Development of General Electric, Schenectady, NY, USA. Since 2003, she has been with the Universidad Carlos III de Madrid, Madrid, Spain, where she is currently an Associate Professor and is with the Group of Power Electronics Systems. In 2016, she stayed as a Visitant Researcher for three months at Tyndall National Institute, Cork, Ireland. She has authored/coauthored more than 100 scientific papers at international conferences and journals, has filed four patents, and is the co-founder of a spin-off company targeting CAD for power electronics. Her research interests include contactless transference of energy, identification techniques applied to switching power converters, design and modeling of high-frequency magnetic components, and design tools for dc/dc converters.

Dr. Fernández has been an Associate Editor for the IEEE TRANSACTIONS ON POWER ELECTRONICS since 2013, and for the IEEE JOURNAL OF EMERGING AND SELECTED TOPICS IN POWER ELECTRONICS since 2019.

Antonio Lázaro (Member, IEEE) was born in Madrid, Spain, in 1968. He received the M.Sc. degree in electrical engineering from the Universidad Politécnica de Madrid, Madrid, Spain, in 1995, and the Ph.D. degree in electrical engineering from the Universidad Carlos III de Madrid, Madrid, Spain, in 2003.

Since 1995, he has been an Assistant Professor with the Universidad Carlos III de Madrid. Since 1994, he has been involved in power electronics, participating in more than 50 research and development projects for industry. He holds seven patents and software registrations and has authored/coauthored nearly 140 papers in IEEE journals and conferences. His research interests include switched-mode power supplies, power factor correction circuits, inverters (railway and grid connected applications), modeling and control of switching converters, and digital control techniques.